

# THE BARYON ACOUSTIC OSCILLATION BROADBAND AND BROAD-BEAM ARRAY: DESIGN OVERVIEW AND SENSITIVITY FORECASTS

JONATHAN C. POBER<sup>1</sup>, AARON R. PARSONS<sup>1</sup>, DAVID R. DEBOER<sup>2</sup>, PATRICK McDONALD<sup>3</sup>, MATTHEW MCQUINN<sup>1,4</sup>, JAMES E. AGUIRRE<sup>5</sup>, ZAKI ALI<sup>1</sup>, RICHARD F. BRADLEY<sup>6,7</sup>, TZU-CHING CHANG<sup>8</sup>, MIGUEL F. MORALES<sup>9</sup>

*Submitted to AJ: 20 Sep 2012*

## ABSTRACT

This work describes a new instrument optimized for a detection of the neutral hydrogen 21cm power spectrum between redshifts of 0.5 – 1.5: the Baryon Acoustic Oscillation Broadband and Broad-beam (BAOBAB) Array. BAOBAB will build on the efforts of a first generation of 21cm experiments which are targeting a detection of the signal from the Epoch of Reionization at  $z \sim 10$ . At  $z \sim 1$ , the emission from neutral hydrogen in self-shielded overdense halos also presents an accessible signal, since the dominant, synchrotron foreground emission is considerably fainter than at redshift 10. The principle science driver for these observations are Baryon Acoustic Oscillations in the matter power spectrum which have the potential to act as a standard ruler and constrain the nature of dark energy. BAOBAB will fully correlate dual-polarization antenna tiles over the 600–900MHz band with a frequency resolution of 300 kHz and a system temperature of 50K. The number of antennas will grow in staged deployments, and reconfigurations of the array will allow for both traditional imaging and high power spectrum sensitivity operations. We present calculations of the power spectrum sensitivity for various array sizes, with a 35-element array measuring the cosmic neutral hydrogen fraction as a function of redshift, and a 132-element system detecting the BAO features in the power spectrum, yielding a  $\sim 2\%$  error on the  $z \sim 1$  distance scale, and, in turn, significant improvements to constraints on the dark energy equation of state over an unprecedented range of redshifts from  $\sim 0.5 - 1.5$ .

*Subject headings:* instrumentation: interferometers — cosmological parameters — distance scale — techniques: interferometric — large-scale structure of the universe

## 1. INTRODUCTION

The Baryon Acoustic Oscillation (BAO) features in the large-scale matter distribution have recently drawn attention as a standard ruler by which the geometry of the universe can be directly measured (Eisenstein et al. 1998, 1999). These features in the cosmic microwave background (CMB) power spectrum and the matter power spectrum today are imprints from the acoustic oscillations in the primordial photon-baryon plasma that recombined at  $z \approx 1100$ . The features in the power spectrum appear at multiples of the sound horizon scale at recombination, making them effective standard rulers. Measuring the BAO wiggles at several redshifts yields geometric measurements of the universe — the Hubble parameter,  $H(z)$ , and the angular diameter distance,  $d_A(z)$  — that constrain properties of the dark energy that dominates the cosmic energy content at  $z = 0$  and is the current leading theory for the accelerated expansion of the universe. Since the first detection of the BAO signal (Eisenstein et al. 2005), several experiments have been undertaken to use these features for precision cosmology,

including the Sloan Digital Sky Survey III Baryon Oscillation Spectroscopic Survey (SDSS-III BOSS; Schlegel et al. 2009)<sup>10</sup>, WiggleZ (Drinkwater et al. 2010)<sup>11</sup>, and the Hobby-Eberly Telescope Dark Energy Experiment (HETDEX; Adams et al. 2011)<sup>12</sup>, as well as a number of planned future experiments, such as the Subaru Prime Focus Spectrograph (PFS; Ellis et al. 2012), Euclid (Amendola et al. 2012), BigBOSS (Schlegel et al. 2011), and the Wide-Field Infrared Survey Telescope (WFIRST)<sup>13</sup>. All of these experiments target individual galaxies with spectroscopic observations.

Rather than targeting individual objects, a 21cm intensity mapping experiment can detect fluctuations in neutral hydrogen emission on large scales (Chang et al. 2008; Wyithe et al. 2008; Morales & Wyithe 2010; Pritchard & Loeb 2011), with two dimensions corresponding to angles on the sky, and the third line-of-sight dimension arising from the differential redshifting of 21cm line emission as a function of distance. After reionization, the power spectrum of 21cm fluctuations is expected to be a biased tracer of the matter power-spectrum, since the remaining neutral hydrogen resides in high-density, self-shielded regions such as in galaxies and other collapsed halos (Barkana & Loeb 2007; Madau et al. 1997). As a result, 21cm intensity mapping experiments present a promising complement to spectroscopic galaxy surveys for BAO science. Several 21cm intensity mapping experiments have been proposed, including the prototype

<sup>1</sup> Astronomy Dept., U. of California, Berkeley, CA

<sup>2</sup> Radio Astronomy Laboratory, U. of California, Berkeley, CA

<sup>3</sup> Physics Div., Lawrence Berkeley National Laboratory, Berkeley, CA

<sup>4</sup> Einstein Fellow

<sup>5</sup> Dept. of Physics and Astronomy, U. of Pennsylvania, Philadelphia, PA

<sup>6</sup> Astronomy Dept. and Dept. of Electrical and Computer Engineering, U. of Virginia, Charlottesville, VA

<sup>7</sup> National Radio Astronomy Observatory, Charlottesville, VA

<sup>8</sup> Institute of Astronomy and Astrophysics, Academia Sinica, Taipei, Taiwan

<sup>9</sup> Dept. of Physics, U. of Washington, Seattle, WA

<sup>10</sup> <http://www.sdss3.org/surveys/boss.php/>

<sup>11</sup> <http://wigglez.swin.edu.au/site/>

<sup>12</sup> <http://hetdex.org/>

<sup>13</sup> <http://wfirst.gsfc.nasa.gov/>

Cylindrical Radio Telescope (CRT; formerly HSHS, Peterson et al. 2006; Seo et al. 2010)<sup>14</sup>, the Canadian Hydrogen Intensity Mapping Experiment (CHIME)<sup>15</sup>, BAORadio (Ansari et al. 2012a,b), the BAO from Integrated Neutral Gas Observations experiment (BINGO; Battye et al. 2012, and an ongoing experiment with the Green Bank Telescope (GBT; Chang et al. 2010).

The flexibility in angular and spectral responses of radio interferometers, which measure the power spectrum both parallel and perpendicular to the line of sight (Morales 2005), gives 21cm BAO the ability to survey larger cosmological volumes and operate over a wider range of redshifts than current spectroscopic galaxy redshift surveys. As a result, the 21cm BAO signal has the potential for probing expansion throughout and beyond the critical epoch when dark energy comes to dominate the energy density of the universe. Furthermore, a 21cm intensity mapping experiment can probe redshifts  $z > 0.5$  with roughly uniform sensitivity, without complications arising from sky emission lines in the optical/near-infrared. The 21cm signal can be used to constrain the location of the BAO peaks as a function of redshift, and thereby measure the magnitude and time-evolution of dark energy.

21cm BAO experiments can draw on the considerable investments in low-frequency radio astronomy developed in the past decade for studies of the Epoch of Reionization (EoR). In this paper, we present the Baryon Acoustic Oscillation Broadband and Broad-beam (BAOBAB) array, a new experiment, building on the legacy of the Precision Array for Probing the Epoch of Reionization (PAPER; Parsons et al. 2010)<sup>16</sup> and the Murchison Widefield Array (MWA; Lonsdale et al. 2009)<sup>17</sup>, for measuring the 21cm HI power spectrum at a redshift of  $z \sim 1$ . This paper is structured as follows: in §2, we present a system architecture for the BAOBAB instrument. In §3, we forecast the sensitivity and cosmological constraints that will be achieved by BAOBAB. We consider several possible challenges and extensions for this approach in §4, and conclude in §5. Throughout this work we assume the WMAP7 best fit  $\Lambda$ CDM cosmological model:  $h = 0.7$ ,  $\Omega_M = 0.27$ ,  $\Omega_b = 0.046$ ,  $\Omega_{DE} = 0.73$ , and  $\sigma_8 = 0.8$  (Larson et al. 2011).

## 2. THE BAO BROADBAND AND BROAD-BEAM ARRAY

The past decade has seen significant progress in the design, construction, and calibration of low-frequency interferometric arrays toward the goal of detecting the highly-redshifted 21cm signal from the Epoch of Reionization. The technologies used in BAOBAB inherit from two EoR experiments — PAPER and the MWA — but with several significant modifications to optimize the instrument for BAO science. The entire signal chain will be re-tuned to operate between 600–900 MHz. These frequencies corresponds to redshifted 21cm emission between  $z = 0.58 - 1.37$ , a band chosen for several reasons. First, these moderate redshifts complement the undergoing lower redshift galaxy surveys like BOSS by probing what is currently a relatively unexplored vol-

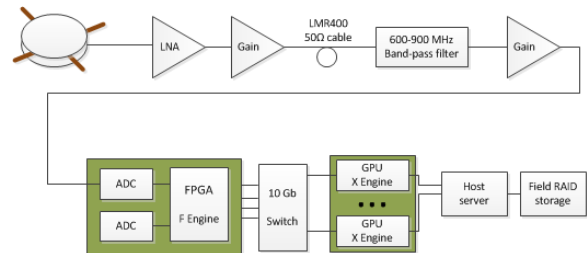


**Figure 1.** System diagram of the BAOBAB interferometer. Dual-polarization antenna signals at -103dBm enter an uncooled low-noise amplifier (LNA) with +12.5dB gain and a noise figure of 0.4dB (30K). Second-stage amplifiers add +36dB gain before transmission through 30 meters of LMR400 50Ω cable to a central enclosure. The signal is bandpass filtered (600–900MHz) and amplified +40dB to the optimal -22dBm input level for the ADCs. Each antenna signal is digitized and channelized in ROACH F-engines, reordered in transmission through a 10Gb Ethernet switch, and sent to GPU GTX580 X-engines for cross-correlation. Raw visibility data are passed to a host computer and written to a RAID storage unit in the MIRIAD UV file format for post-processing.

ume of the universe. Secondly, at these frequencies, commercially available amplifiers and cables provide suitable low-noise performance that would not be obtainable at higher frequencies (lower redshifts). Furthermore, this band also avoids the bright sky noise and ionospheric effects that complicate lower frequency (higher redshift) observations.

BAOBAB will be a non-phase-tracking, broadband array of beam-formed tiles. By lowering the field-of-view of each element, the use of beamformed tiles like the MWA will significantly increase BAOBAB’s power spectrum sensitivity over that of an array of the equivalent number of single dipoles, without increasing the correlator demands. Each tile will consist of 4 scaled versions of the PAPER sleeved-dipole design and groundscreens, electronically beamformed to point to zenith. Two linear polarization signals from each tile enter a digital signal processor that computes both auto- and cross-correlation products and outputs the results locally to disk. A block diagram is given in Fig. 1; the key properties of the BAOBAB system are listed in Table 1 and are described in more detail in the remainder of this section.

**Table 1**  
Proposed BAOBAB Array

Operating Bandwidth	600–900 MHz
Number of Tiles	32–128
Collecting Area per Element	2.6 m <sup>2</sup>
Gain per Element	18 dBi
Field-of-View	0.045 str
Receiver Noise Temperature	40 K
System Temperature	50 K
Maximum Imaging Baseline	60 m
Redundant Baseline Scale	1.6 m
$k_{\min}, k_{\max}$	0.01, 2.5 $h\text{Mpc}^{-1}$
Array Configuration	Reconfigurable (see Fig. 6)
Frequency Resolution	300 kHz
Snapshot Integration Time	10 s

### 2.1. Siting

Since radio-frequency interference (RFI) is prevalent at these frequencies, BAOBAB will need to be located at a radio quiet site. The bottom panel of Figure 2 shows pre-

<sup>14</sup> <http://cmb.physics.wisc.edu/people/lewis/webpage/>

<sup>15</sup> <http://www.mcgillcosmology.ca/chime>

<sup>16</sup> <http://eor.berkeley.edu/>

<sup>17</sup> <http://www.mwatelescope.org/>

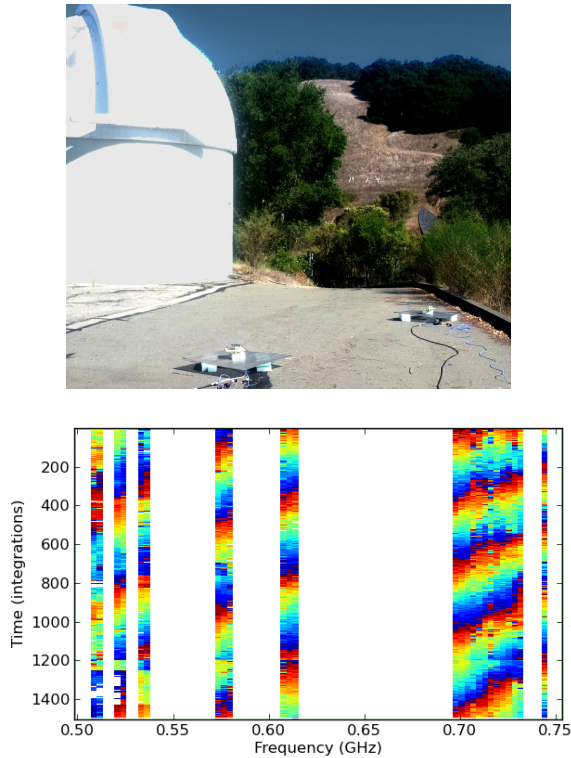


**Figure 2.** *Top:* Leuschner Observatory, with a prototype 2-element BAOBAB interferometer deployed. This system was developed and deployed by students as part of a *Fundamentals of Radio Astronomy* class at UC Berkeley. *Bottom:* solar fringes measured with the BAOBAB-2 prototype at Leuschner.

liminary measurements made by a prototype 2-antenna BAOBAB interferometer deployed at the Leuschner Observatory near Berkeley, CA. At this site, only 40 MHz of a 400–800 MHz operating band show solar fringes uncorrupted by RFI, demonstrating the need for the primary BAOBAB deployment to be located at a quieter site, such as the NRAO site near Green Bank, WV. Next-generation activities may take place at the Square Kilometer Array South Africa (SKA-SA) reserve in the Karoo desert. This site is currently occupied by the PAPER and MeerKAT arrays, and has been shown to be a pristine RFI environment (Jacobs et al. 2011).

## 2.2. Analog System

With the drastic reduction in sky noise relative to EoR frequencies, BAOBAB’s system temperature will be dominated by the analog electronics. These components must therefore be optimized to reduce receiver noise while maintaining the smooth spatial and spectral responses that are a hallmark of the PAPER design and a key component of the delay spectrum foreground isolation approach presented in Parsons et al. (2012b) (hereafter P12b) and discussed in §3.3. The analog system will include the collecting element (consisting of 4 antennas and reflectors), low-noise amplifier, coaxial cable, and receiver.

The BAOBAB element will begin with a 1/5-scale PAPER antenna (Parsons et al. 2010), as shown in Figure 3. This design is a dual-polarized version of the sleeved dipole design that uses a twin-resonance structure consisting of a pair of crossed dipoles located between a pair of thin aluminum disks. The element’s reliability has

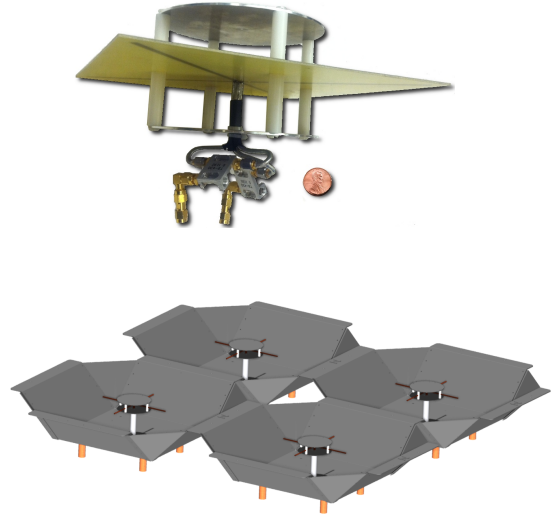


**Figure 3.** *Top:* A prototype BAOBAB dipole antenna, designed as a 1/5 scale model of a PAPER dipole. *Bottom:* BAOBAB tile design with 4 dipoles and individual ground-screens.

been demonstrated in PAPER arrays over the past several years. A trough reflector under each dipole will be used to increase the directivity toward zenith. The electromagnetic behavior of the element was modeled extensively for PAPER using CST Microwave Studio, and shown to perform as desired through calibration with celestial sources in Pober et al. (2012). The geometrically re-tuned prototype shown in the top panel of Figure 3 will be optimized to operate efficiently over the 600–900 MHz band.

Rather than deploy single elements like PAPER, BAOBAB will use a  $2 \times 2$  tile of dipoles and ground-screens, as shown in Figure 3. A fixed zenith beam-former will be used to combine the signals, increasing the gain by 6 dB and reducing the field-of-view by a factor of four. Both analog and digital beamformers are being investigated. A key issue is the mutual coupling, which should be reduced by the additional groundscreens between dipoles. The net effect is that for a fixed correlator size, the power-spectrum sensitivity is increased by a factor of four (see §3.2).

The amplifier designed for PAPER has a measured noise temperature of 110 K with 30 dB of gain across the 120–170 MHz band (Parsons et al. 2010). For application to BAO at  $z \sim 1$ , we will modify this amplifier design to operate from 600–900 MHz. Besides re-tuning the filter and amplifier circuits, however, one of the major activities in this modification will be to reduce the noise temperature of the front-end amplifier in order to obtain a target system temperature of 50 K. This change reflects one of the key differences between the BAO and EoR foregrounds. System noise in the EoR band is dominated by  $\sim 300$  K sky noise from galactic synchrotron emission. In the BAO band, the sky temperature is reduced to  $\sim 10$  K, making the front-end amplifier the leading source of noise. Uncooled commercial UHF-band amplifier transistors based on GaFET or HEMT technology can reliably achieve noise figures of 0.4 dB, corresponding to a receiver temperature of 30 K. A prototype BAOBAB balun/amplifier using a Hittite HMC617LP3 LNA with



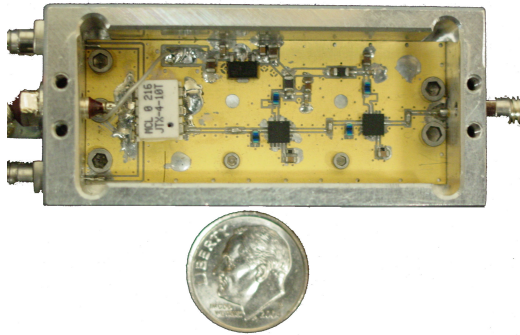


**Figure 4.** The prototype balun and Hittite HMC617LP3 LNA for BAOBAB. The amplifier adds +30dB of gain with a quoted noise figure of 0.5 dB.



**Figure 5.** PAPER's 128-input correlator (shown) follows the packetized frequency-cross-multiply (FX) architecture developed by the Center for Astronomy Signal Processing and Electronics Research (CASPER). Shown are 16 ROACH F-engines (left) and 2 dual-GPU box X-engines (right). The first-generation BAOBAB correlator will modify the 64-input, 100-MHz PAPER correlator to become a 32-input, 300-MHz correlator. It will employ eight ROACH boards for spectral processing and four dual-GPU boxes for cross-multiplication. A 10-GbE switch is used to route data between boards.

a quoted noise figure of 0.5 dB is shown in Figure 4; tests are underway to determine the noise temperature of the complete system.

### 2.3. Digital System

The BAOBAB correlator will follow the scalable correlator design used by PAPER and other members of the international Collaboration for Astronomy Signal Processing and Electronics Research (CASPER)<sup>18</sup>, a real-time digital correlator based on Field-Programmable Gate Array (FPGA) processors and graphics processing units (GPUs) (Parsons et al. 2008; Clark et al. 2011). The correlator architecture we employ uses modular signal processing electronics and packetized communication protocols to build correlators that are flexible in the number of antennas correlated and the bandwidth correlated by each antenna. A photograph of a 128-input FPGA/GPU correlator is shown in Fig. 5.

The generic FX correlator architecture we implement consists of modules responsible for digitizing and chan-

nelizing each set of antenna inputs (F-Engines), followed by a set of signal processing modules responsible for cross-multiplying all antennas and polarizations for a single frequency (X-Engines) and accumulating the results. Unique to this architecture, signal processing engines transmit packetized data through commercially available 10 Gb Ethernet switches that are responsible for routing data between boards. This architecture, along with analog-to-digital converters, modular FPGA-based signal processing engines, and a software environment for programming, debugging, and running them, were developed in collaboration with CASPER at the University of California, Berkeley (Parsons et al. 2008). The flexibility and modularity of this correlator design shortens development time, and in this case, allows an existing 64-input, 100-MHz PAPER correlator with 8 ROACH-boards and 4 dual-GPU boxes to be straight-forwardly modified to become a 32-input, 300-MHz BAOBAB correlator using the same boards and signal processing libraries. A forthcoming publication on this correlator will be presented in Ali et al. (2013).

### 2.4. Configuration

BAOBAB will employ small antennas and above-ground cabling with relatively inexpensive LMR400 50-Ohm coaxial cables; these cables will not be buried, allowing BAOBAB to easily change between different array configurations by moving antenna elements. Following the principles outlined in (Parsons et al. 2012a, hereafter P12a), BAOBAB will employ a minimum-redundancy imaging configurations for characterizing foregrounds with minimal sidelobes and maximum-redundancy configurations to repeatedly sample the same locations in the uv-plane, substantially improving sensitivity to the three-dimensional power spectrum of 21cm emission at  $z \sim 1$ . Although future experiments may target a range of angular scales to map 21cm emission in the plane of the sky, by focusing on a limited number of Fourier modes, these maximum-redundancy configurations can improve sensitivity to the power spectrum by an order of magnitude or more in  $\text{mK}^2$ , relative to an equivalent observation with a minimum-redundancy configuration.

However, as will be discussed further in §3.2.1, the mapping of baseline length to a transverse  $k$ -mode on the sky is significantly larger for BAOBAB than for PAPER. In order to probe the relatively large-scale BAO features, then, BAOBAB will use the most compact configurations possible for its power spectrum measurements. Such an array configuration for a 35-element system, as well as that of a 32-element imaging configuration, are shown in Figure 6. The tiles are spaced 1.6m apart, effectively touching end-to-end. Investigations of cross-talk and mutual coupling will take place during an early prototype of the system; it may be the case that a phase-switch or additional shielding between tiles will be necessary to accommodate the short baselines required by BAO science.

With a modular CASPER correlator increasingly able to process larger numbers of antenna inputs, BAOBAB naturally lends itself to a staged approach. Early  $\leq 16$  tile-element prototypes will characterize system performance, while a subsequent  $\sim 32$ -element array will study foreground emission and constrain the neutral hydrogen fraction as a function of redshift with a measurement of the 21cm power spectrum (§3.4). A  $\sim 128$ -tile version of

<sup>18</sup> <https://casper.berkeley.edu>

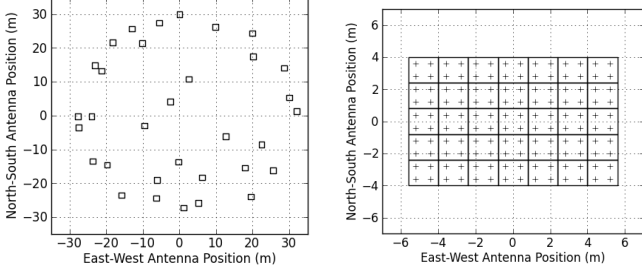


**Figure 6.** BAOBAB array configurations, plotted in meters east-west (horizontal axis) and north-south (vertical axis). BAOBAB will use above-ground cabling to allow antennas to be moved into a minimum-redundancy configuration (left) for imaging foregrounds, or a maximum-redundancy configuration (right) for enhanced power-spectrum sensitivity. Each square represents one tile, and each “+” one dipole.

BAOBAB will measure BAO features and provide substantial improvements over our current constraints on the equation of state and time evolution of dark energy (§3.5).

### 3. PREDICTED COSMOLOGICAL CONSTRAINTS FROM BAOBAB

In this section we present predictions for forthcoming cosmological constraints for several iterations of the BAOBAB instrument. We begin by reviewing the predicted signal strength for the cosmological 21cm power spectrum in §3.1. In §3.2, we adapt the power spectrum sensitivity calculations of P12a for an array operating at  $z \sim 1$ , including the effects of sample variance and shot noise. In 3.3, we briefly review the delay spectrum foreground removal procedure of P12b. While a detailed study of foregrounds is beyond the scope of this paper, it is worthwhile to discuss the implications of the technique on which Fourier modes of the 21cm power spectrum will be accessible. We conclude the section by presenting forecasts for a 35- and 132-element BAOBAB system in §3.4 and §3.5 respectively, including Fisher matrix predictions for constraints on the dark energy equation of state in the latter section. In the discussion of §4, we explore possible directions for improvement with larger BAOBAB arrays.

#### 3.1. The 21cm Power Spectrum

As with galaxy redshift surveys, a 3D map of the neutral hydrogen in the universe will serve as a tracer of the underlying dark matter power spectrum. The brightness of the observable radio 21cm signal will depend on the cosmological neutral hydrogen fraction, as well as the bias of hydrogen containing haloes with respect to the dark matter (Barkana & Loeb 2007; Madau et al. 1997; Ansari et al. 2012b):

$$P_{T_{21}}(k, z) = \left[ \tilde{T}_{21}(z) \right]^2 b^2 P(k, z), \quad (1)$$

$$\tilde{T}_{21}(z) \simeq 0.084 \text{mK} \frac{(1+z)^2 h}{\sqrt{\Omega_m(1+z)^3 + \Omega_\Lambda}} \frac{\Omega_B}{0.044} \frac{f_{\text{HI}}(z)}{0.01}, \quad (2)$$

where  $\tilde{T}_{21}(z)$  is the mean 21cm brightness temperature at redshift  $z$ ;  $P(k, z)$  is the linear matter power spectrum;  $b$  is the bias factor of HI containing halos with

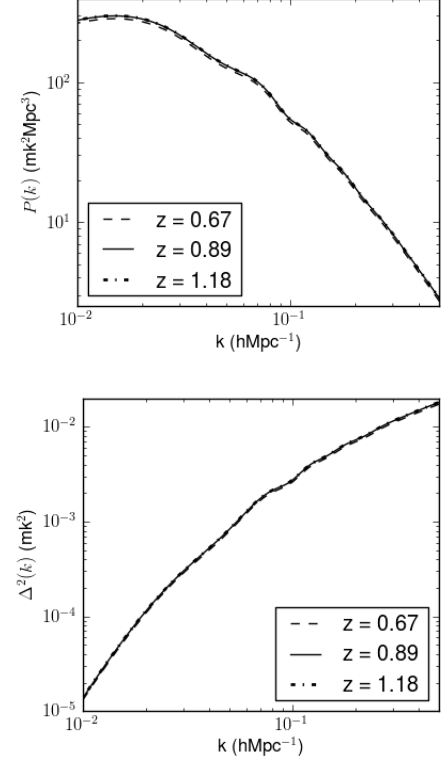


**Figure 7.** *Top:* The predicted power spectrum of 21cm emission in our fiducial model at three redshifts: 0.67, 0.89 and 1.18 (corresponding to frequencies of 850, 750 and 650 MHz). The  $z = 0.89$  and  $z = 1.18$  power spectra overlap, and, effectively, the signal is at the same strength for all three redshifts. Matter power spectrum predictions come from CAMB. *Bottom:* The equivalent dimensionless power spectra,  $\Delta^2(k) = \frac{k^3}{2\pi^2} P(k)$ .

respect to the dark matter;  $f_{\text{HI}}(z)$  is the mass fraction of neutral hydrogen with respect to the overall cosmological baryon content (i.e.,  $\Omega_{\text{HI}} = f\Omega_b$ );  $\Omega_\Lambda$  is the cosmological constant, and  $\Omega_m$  and  $\Omega_B$  are the matter and baryon density in units of the critical density, respectively.

We plot the predicted 21cm brightness temperature power spectrum,  $P(k)$ , for our fiducial model at redshifts of 0.67, 0.89 and 1.18 (corresponding to frequencies of 850, 750, and 650 MHz, respectively) in Figure 7. Predictions for the matter power spectrum come from CAMB (Lewis et al. 2000)<sup>19</sup>. We also plot the dimensionless power spectrum,  $\Delta^2(k) = \frac{k^3}{2\pi^2} P(k)$ . For the remainder of this paper we will primarily express our results in terms of  $\Delta^2_{T_{21}}(k)$ , due to its more intuitive units ( $\text{mK}^2$ ) and simple physical interpretation as the variance per logarithmic  $k$  bin.

In practice, the 21cm power spectrum is measured in redshift space, which can be, at linear order, related to the real-space  $P_{T_{21}}(k, z)$  as (Kaiser 1987):

$$\tilde{P}_{T_{21}}(k, z) = (1 + \beta\mu^2)^2 P_{T_{21}}(k, z) \quad (3)$$

where  $\mu = \hat{k} \cdot \hat{z}$  is the wavevector  $\hat{k}$  projected along the line-of-sight  $\hat{z}$ , and  $\beta \equiv f(\Omega)/b$  from linear theory where  $f(\Omega) \approx \Omega_m(z)^\gamma$  is the dimensionless linear growth rate and  $\gamma = 0.557$  for  $\Lambda$ CDM cosmologies. To incorporate

<sup>19</sup> <http://camb.info/>

the effects of redshift-space distortions in the following calculations, we reduce our thermal noise error bars in  $k$ -space by the factor of  $(1 + \beta\mu^2)^2$ ; however, we do not attempt to constrain cosmological parameters like  $\beta$  by measuring the power spectrum as a function of  $\mu$ . We assume fiducial values of  $f_{\text{HI}} = 0.015$  and  $b = 0.75$ , chosen to agree with  $f_{\text{HI}}b = 0.012 \pm 0.003$  as measured by Chang et al. (2010). To obtain individual constraints on these parameters, one will need to measure redshift-space distortions themselves.

### 3.2. Sensitivity of an Array to the 21cm Signal

There are three independent sources of statistical uncertainty in a 21cm power spectrum measurement: thermal noise in the interferometric visibilities, sample variance, and shot noise, of which the last is in some sense “signal,” but still inhibits measurements of cosmological parameters. For the first-generation of 21cm experiments, thermal noise will be the dominant source of uncertainty in measurements of the power spectrum. We therefore calculate the effects of thermal noise independently in §3.2.1. We add in the effects of sample variance in §3.2.2 and argue in §3.2.3 that shot noise can be neglected for these experiments.

#### 3.2.1. Thermal Noise

Thermal noise, in addition to being the dominant source of uncertainty in first generation 21cm BAO experiments, is also likely to be least familiar to those used to optical redshift surveys. Given the limited collecting area of early experiments, reducing thermal noise contributions is of paramount importance, even at the expense of the number of Fourier modes measured. Much of the work in this section builds off of the derivation of an interferometric array’s power spectrum sensitivity presented in P12a. We begin with a version of their equation 16, which gives the power spectrum of the thermal noise obtained from one integration of a dual-polarization baseline:

$$\Delta_N^2(k) \approx X^2 Y \frac{k^3}{2\pi^2} \frac{\Omega}{2t} T_{\text{sys}}^2, \quad (4)$$

where  $X^2 Y$  is a scalar translating observed units to cosmological distances in  $h^{-1}\text{Mpc}$  ( $X$  converts from angles on the sky to transverse distances,  $Y$  from bandwidth to line-of-sight distance),  $\Omega$  is the solid angle of the primary beam of one element in steradians, and  $T_{\text{sys}}$  is the system temperature.

The science goals of a BAO experiment are to actually measure  $X$  and  $Y$ ; that is, since the exact values of  $X$  and  $Y$  depend on the underlying cosmology, we can combine the known physical scale of BAO with the angular and frequency scales in the observed signal to extract the detailed expansion history of the universe. For the purpose of a sensitivity derivation, however, the behavior of  $X$  and  $Y$  can be considered well enough known to compute fiducial values.

$X$  is related to the angular size distance,  $D_A$ , as

$$X = D_A(1+z) \equiv \int_0^z \frac{c \, dz}{H(z)}, \quad (5)$$

with  $H(z)$  in the matter/dark-energy dominated epoch being approximately given by

$H(z) = H_0 \sqrt{\Omega_M(1+z)^3 + \Omega_\Lambda}$ . Numerical integration for a flat universe with  $\Omega_M = 0.27$ ,  $\Omega_\Lambda = 0.73$ , and  $H_0 = 70$  yields  $D_A(z=1) \approx 1680$  proper Mpc (Wright 2006). Ignoring the evolution in the angular diameter distance around  $z \sim 1$ , we can write:

$$X \approx 1700(1+z) \frac{\text{Mpc}}{\text{radian}}. \quad (6)$$

Note that although we use this (admittedly somewhat poor) approximation for simplicity in deriving the relations for thermal noise power spectra in this subsection, all the subsequent results include the full  $z$ -dependence of the angular diameter distance.

A few more words are warranted concerning the magnitude of  $X$  at  $z = 1$ . Given the scaling of equation 5, a  $16\lambda$ -baseline (6.8m at  $z = 1$ ) corresponds to a transverse wavemode of  $k_\perp = 0.042 \, h\text{Mpc}^{-1}$ , a non-negligible value compared to the first BAO peak at  $\sim 0.08 \, h\text{Mpc}^{-1}$ . Therefore, baselines longer than  $\sim 32\lambda$  will lose access to the first peak and be less effective probes of cosmology, regardless of foreground effects to be discussed later. This scaling motivates the extremely compact configurations proposed for BAOBAB in §2, despite the possible systematics associated with such short baselines.<sup>20</sup>

To compute the scaling between frequency,  $\nu$ , and comoving line-of-sight distance,  $r_{\text{los}}$ , we use

$$dr_{\text{los}} = \frac{cdz}{H(z)}. \quad (7)$$

Since  $\nu(1+z) = \nu_{21}$ , we have that  $dz/(1+z) = -d\nu/\nu$ , so

$$Y \equiv \frac{dr_{\text{los}}}{d\nu} = \frac{c(1+z)^2}{\nu_{21}H(z)}. \quad (8)$$

Evaluating the above numerically, we get

$$Y = 3.0 \frac{(1+z)^2}{\sqrt{\Omega_M(1+z)^3 + \Omega_\Lambda}} \frac{\text{Mpc}}{\text{MHz}}. \quad (9)$$

Finally, we compute the product  $X^2 Y$  used in equation 4:

$$X^2 Y \approx 2.93 \frac{(1+z)^4}{\sqrt{\Omega_M(1+z)^3 + \Omega_\Lambda}} \frac{(h^{-1}\text{Mpc})^3}{\text{sr} \cdot \text{Hz}}. \quad (10)$$

Nominally,  $X^2 Y = 28(h^{-1}\text{Mpc})^3 \text{sr}^{-1} \text{Hz}^{-1}$  at  $z = 1$ .<sup>21</sup>

The other values in equation 4 are system-dependent parameters. The BAOBAB tiles have a considerably sized primary beam on the sky,  $\Omega \approx 150\text{sq.deg} \approx 0.045\text{sr}$ . However, this beam is significantly narrower than that of a single dipole, so that the use of beamforming results

<sup>20</sup> Epoch of Reionization experiments at  $z = 9$ , however, do not find themselves limited by the transverse modes probed.  $X(z=9) \approx 9360 \frac{\text{Mpc}}{\text{radian}}$  (P12a), so that a  $16\lambda$ -baseline corresponds to  $k_\perp = 0.015 \, h\text{Mpc}^{-1}$ . With this scaling, the effect of the  $k_\perp$  component on the measured power spectrum will always be sub-dominant to the foreground effects described in P12b.

<sup>21</sup> The magnitude of  $X^2 Y$  at  $z = 1$  represents an often underappreciated gain in sensitivity between a 21cm BAO experiment and a similar reionization experiment. At  $z = 9$ ,  $X^2 Y \approx 540(h^{-1}\text{Mpc})^3 \text{sr}^{-1} \text{Hz}^{-1}$ , meaning that the quoted EoR signal strength of  $\sim 10\text{mK}^2$  is normalized over a much larger volume. The smaller volume scalar at  $z = 1$  means that over an order of magnitude less thermal noise is picked up per equivalent integration.

in a considerably lower noise level, since our noise power spectrum scales as  $\Omega$  into equation 4.

The issue of system temperature is another instance where a BAO experiment at  $z = 1$  is fundamentally different from an EoR experiment at  $z = 9$ . In the EoR case, Galactic synchrotron emission is the primary source of noise at 150 MHz, with a value of  $\sim 300\text{K}$  toward the galactic poles. However, synchrotron emission scales approximately as

$$T_{\text{sync}} \approx 300\text{K} \left( \frac{\nu}{150\text{MHz}} \right)^{-2.5}. \quad (11)$$

At frequencies around 750 MHz,  $T_{\text{sync}} \approx 5\text{K}$ . This value is substantially below typical receiver temperatures of 50K, so that receiver temperatures will dominate  $T_{\text{sys}}$ . As described in §2, BAOBAB will have a system temperature of approximately 50K across its entire band.

We can express the noise power spectrum of one dual-polarization baseline integrating on one Fourier mode by substituting these fiducial values in equation 4:

$$\begin{aligned} \Delta_N^2(k) \approx & 8 \times 10^{-3} \frac{(1+z)^4}{\sqrt{\Omega_M(1+z)^3 + \Omega_\Lambda}} \\ & \times \left[ \frac{k}{0.1 \text{ hMpc}^{-1}} \right]^3 \left[ \frac{\Omega}{0.045 \text{ sr}} \right]^{\frac{3}{2}} \\ & \times \left[ \frac{180 \text{ days}}{t_{\text{days}}} \right] \left[ \frac{|\vec{u}|}{20} \right] \left[ \frac{T_{\text{sys}}}{50 \text{ K}} \right]^2 \text{ mK}^2, \end{aligned} \quad (12)$$

where  $|\vec{u}|$  is the length of the baseline in wavelengths. The additional factors of  $\Omega^{\frac{1}{2}}$  sets the diameter of a  $uv$ -pixel and  $|\vec{u}|$  sets the length of time the baseline samples that same pixel. Our fiducial “long observation” is 180 days; we set this value as a hard maximum for the number of days BAOBAB can observe in one calendar year. This choice comes from the fact that observations will be compromised by foreground emission when either the Galactic plane or the sun is in view.

In order to calculate the sensitivity of an entire interferometric array, we must sum the contributions of all the Fourier modes sampled every baseline, paying careful attention to the number of times a unique Fourier mode is sampled by distinct redundant baselines. In our formalism, the effect of array configuration enters through the  $f/f_0$  metric for the amount of redundancy in an array configuration, defined in P12a as:

$$\frac{f}{f_0} \equiv \frac{\sum_i n_i^2}{\sum_i n_i}, \quad (13)$$

where  $i$  labels individual  $uv$  pixels, and  $n_i$  the number of one-second integration samples falling within pixel  $i$ . An  $f/f_0$  factor of  $10^4$  is representative of the 32-element maximum redundancy arrays also described in P12a. The sensitivity boost comes from the fact that redundant sampling beats down thermal noise more quickly, since redundant measurements can be added in temperature, whereas distinct modes with the same  $|\vec{k}|$  can only be added in the temperature-squared units of a power

spectrum. The resultant sensitivity is:

$$\begin{aligned} \Delta_N^2(k) \approx & 2 \times 10^{-4} \frac{(1+z)^4}{\sqrt{\Omega_M(1+z)^3 + \Omega_\Lambda}} \\ & \times \left[ \frac{k}{0.1 \text{ hMpc}^{-1}} \right]^3 \left[ \frac{\Omega}{0.045 \text{ sr}} \right] \left[ \frac{T_{\text{sys}}}{50 \text{ K}} \right]^2 \\ & \times \left[ \frac{8 \text{ hrs}}{t_{\text{per\_day}}} \right]^{\frac{1}{2}} \left[ \frac{180 \text{ days}}{t_{\text{days}}} \right] \left[ \frac{32}{N} \right] \left[ \frac{10^4 f_0}{f} \right]^{\frac{1}{2}} \text{ mK}^2. \end{aligned} \quad (14)$$

The  $f/f_0$  term is computed from  $uv$  sampling patterns including earth rotation aperture synthesis effects, and accounts for most all effects regarding array configuration. Hence, the additional factors of  $\Omega^{\frac{1}{2}}$  and  $|\vec{u}|$  that appeared in equation 12 do not appear in 14. However, we have separated the term containing  $N$ , the number of antennas, to give a sense of how sensitivity will roughly scale with array size. The factor of  $t_{\text{per\_day}}$  sets the total integration time per day, which will likely be limited by the size of a low foreground emission region (i.e., a “cold patch”). We choose 8 hours as the maximum time that can spent observing cold patches per day, a value influenced by existing all-sky maps and observations with PAPER. To calculate  $f/f_0$ , we split this 8-hour period into separate one-hour observations phased to a single pointing center, roughly corresponding to the width of the BAOBAB primary beam, after which a statistically independent patch of sky comes to dominate the data.

### 3.2.2. Sample Variance

In galaxy redshift surveys, the sample variance can be calculated relatively simply by counting Fourier modes over an effective survey volume. However, in the case of BAOBAB, not all modes are equal, since we have used redundant samples of certain modes to beat down thermal noise. In creating a 1- or 2-D power spectrum out of the full 3-D Fourier space, we must take a weighted combination of these modes, since the ratio of thermal noise to sample variance can vary between every  $k$ -mode measured.

Using inverse-variance weighting to combine each measurement at a particular  $k$ -mode, one finds that the optimal estimator of the power spectrum results in an error that can be calculated by combining the errors on each separate mode in inverse-quadrature:

$$\delta\Delta^2(k) = \left( \sum_i \frac{1}{(\Delta_{N,i}^2(k) + \Delta_{21}^2(k))^2} \right)^{-\frac{1}{2}}, \quad (15)$$

where  $\delta\Delta^2(k)$  is the resultant uncertainty on a given  $k$ -mode,  $\Delta_N^2$  is the thermal noise power spectrum calculated in 3.2.1,  $\Delta_{21}^2(k)$  is the cosmological 21cm power spectrum (which is also the sample variance error), and  $i$  is an index labeling the independent  $k$ -modes over which we are summing (note that we never combine modes into bands with significantly varying  $\mathbf{k}$ , which is why we can sum inverse absolute variance instead of inverse fractional variance).

Since the sample variance is completely a function of the  $uv$ -coverage of an array, it is best calculated numeri-

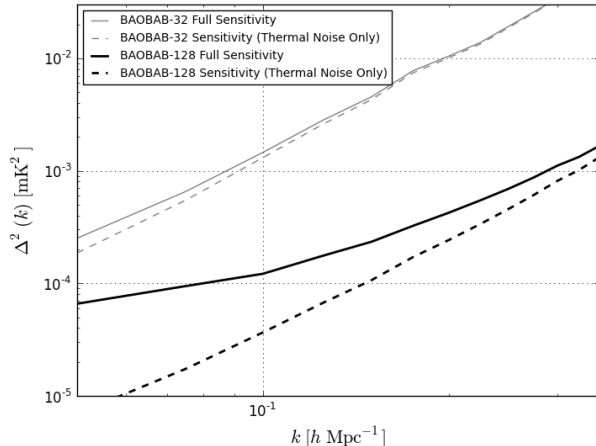


**Figure 8.** Noise levels for two fiducial observations of one declination range with BAOBAB. The dashed gray (black) line shows the sensitivity given thermal noise only for a 30 days observation with a 35-element system (180 days with a 132-element system); solid lines show the effect of including sample variance. At the larger scales, the 180 day observation with 132-tiles is completely dominated by sample variance. At the smaller scales, the analytic expression for thermal noise given in equation 14 accurately reproduces the sensitivity. The plotted thermal noise only curve is not a perfect power-law because longer baselines cannot probe the largest scale  $k$ -modes. To be more realistic, the foreground model discussed in §3.3 is used to exclude contaminated modes from the sensitivity calculation, which also affects the thermal noise predictions at the largest scale modes.

cally. In Figure 8 we plot the 1D thermal noise and sample variance uncertainties for two maximum-redundancy configurations of BAOBAB — 35- and 132-tiles — shown in Figures 6 and 10. To calculate the sample variance, we use the 21cm brightness power spectrum from CAMB, shown in Figure 7. At the scale of the first acoustic peak, sample variance has clearly become the dominant source of error for a long integration with 132-elements; we discuss possible methods for improving this situation in §3.5 and §4.2. At the smaller scales, however, the analytic functions given in the previous section accurately reproduce the array sensitivity. Note that the thermal noise only curve in Figure 8 is not a perfect power law because not all baselines can probe the largest scales. Also note that the foreground model discussed in §3.3 is used to exclude modes from this calculation.

### 3.2.3. Shot Noise

Measurements of the 21cm power spectrum will also be affected by the discrete nature of the neutral hydrogen distribution at low redshift. Only overdensities self-shielded to the  $\sim 1$  Ry ionizing background contain neutral hydrogen, so we will be subject to the same galactic shot noise as optical redshift surveys. Following Seo et al. (2010), we assume that galaxy positions and luminosities are distributed with probability proportional to  $1 + b \delta_m$ , where  $b$  is the bias and  $\delta_m$  is the mass overdensity. This allows us to treat shot noise as a scale-independent contribution to the power spectrum with  $P(k) = 1/\bar{n}$ . In terms of 21cm brightness:

$$\Delta_{\text{shot}}^2(k) \approx \left[ \tilde{T}_{21}(z) \right]^2 \frac{1}{\bar{n}} \frac{k^3}{2\pi^2} \quad (16)$$

Using the result of Seo et al. (2010) (who use a fit to the neutral hydrogen mass function of Zwaan et al. 2005),  $\bar{n} = 0.01 \, h^3 \text{Mpc}^{-3}$  and  $\Delta_{\text{shot}}^2 \approx 6.5 \times 10^{-5} \text{mK}^2$  at  $k = 0.1 \, h \text{Mpc}^{-1}$  and  $z = 1$ . The number density of hydrogen-containing halos is substantially higher than for the bright galaxies used in optical/NIR surveys, making shot noise a substantially smaller contaminant; it will only begin to dominate the signal at  $k > 2 \, h \text{Mpc}^{-1}$ . Regardless of uncertainties in this calculation, shot noise is clearly a subdominant effect, and we neglect it for the remainder of this work.

### 3.3. The Delay Spectrum Technique at $z \sim 1$

Before combining the results of the last two sections, we must discuss the effect of foregrounds on power spectrum measurements. The presence of foreground emission orders of magnitude brighter than the cosmological 21cm signal has been one of the major impediments for high-redshift 21cm tomography. P12b presented a per-baseline delay-spectrum technique for isolating foreground emission solely on the basis of its spectral smoothness. In this section we briefly recapitulate the principles of the delay-spectrum technique, and present a simple approximation for the behavior of foregrounds in the 600-900 MHz band.

The delay spectrum technique is a methodology for using each baseline of an interferometer as a independent probe of the 21cm power spectrum. The most powerful aspect of this approach is that the frequency dependence of a baseline’s Fourier sampling pattern, typically regarded as a major complication for 21cm experiments, naturally gives rise to an isolation of foreground emission in Fourier space. The ability to remove foregrounds on a per-baseline basis allows multiple baselines to be tuned to target the same Fourier mode for greater sensitivity, as opposed to more traditional techniques that use overlapping  $uv$ -coverage at multiple frequencies to avoid the issue of frequency-dependent sampling.

At the heart of the delay transform is a dual interpretation of the Fourier transform of interferometric visibilities along the frequency axis. On the one hand, for 21cm experiments, frequency maps directly into redshift since the observed signal is a spectral line. Therefore, the Fourier transform along the frequency axis gives  $k_{\parallel}$ , the Fourier wavemode along the line of sight. However, the frequency dependence of a baseline’s length (as measured in wavelengths), gives rise to the delay transform interpretation of the frequency Fourier transform presented in Parsons & Backer (2009). If performed over a wide enough bandwidth, this transform maps sources to Dirac delta functions in “delay space,” corresponding to the geometric delay of signal arrival time between the two elements of the baseline. There is thus a maximum delay at which any signal coming from the sky can appear, set by the physical length of the baseline. Furthermore, each source delta-function will be convolved by a kernel representing the Fourier transform of that source’s intrinsic spectrum (as well as any spectral features introduced by the instrument). Therefore, as long as the instrumental frequency structure is kept to a minimum, sources with smooth intrinsic spectra (such as foreground emission) will have their emission confined within the region of delay space set by the maximum delays (the so-called



“horizon-limit”). Sources with unsmooth emission, like the 21cm signal, will be convolved by a broad kernel, scattering “sidelobes” well beyond the horizon limit, and creating a window for detecting 21cm emission free of smooth-spectrum foregrounds.

A full simulation quantifying the effects of the delay transform on foregrounds is beyond the scope of this work. Rather, we assign a baseline-dependent minimum  $k_{\parallel}$ , below which we exclude modes as being wholly contaminated by foregrounds. We chose the value of  $k$  based on the simulations presented for PAPER in Parsons et al. (2012b), which finds for the shortest baselines foregrounds contaminate modes with  $k_{\parallel} \lesssim 0.2 \text{ hMpc}^{-1}$ . At EoR frequencies of 150 MHz, this cutoff maps to delay-modes of 400 ns. Since BAOBAB baselines are physically shorter by a factor of 5, this reduces the maximum delay-space contamination to 80 ns, which in turn maps back to  $k = 0.1 \text{ hMpc}^{-1}$  at 750 MHz, using the  $Y$  parameter from equation 8. There are two important factors which will further serve to reduce this number for BAOBAB. First, celestial foregrounds should have power law spectra with steeply decrease in intensity versus frequency, and so will be fainter than at EoR frequencies. Although the signal has also fallen a similar amount, this reduced foreground structure will still make the delay transform even more effective at isolating foreground emission. Secondly, the narrower primary beam of BAOBAB will limit the delay modes from which there can be appreciable celestial emission, as sources near the horizon will be significantly attenuated.

We perform a cursory calculation in which the delay-transform is applied to a simulated sky model. In these simulations, we assume the sky is entirely composed of point sources, where the source strength distribution follows a power-law with a slope of -2.0, normalized to a 2 Jy source per 10 steradians, a distribution derived empirically from PAPER data with extrapolation to the BAOBAB band. We also model the frequency spectrum of each source as a power-law with a normal distribution of spectral indices centered on -1.0 and a standard deviation of 0.25. We refer to these simulations as “cursory,” since they exclude instrumental effects such as RFI flagging and frequency-dependent beam structure. Instead, we use a single, frequency-independent Gaussian to model the primary beam of the BAOBAB tile; the potential effects of a more realistic beam model are discussed in §4. We find the delay transform confines foregrounds to  $k$ -modes below a value of  $k_{\parallel} = 0.045 \text{ hMpc}^{-1}$  for baselines of 16 wavelengths. The  $k_{\parallel}$  value for the maximum delay of a  $16\lambda$  baseline at 750 MHz (i.e., the horizon limit) is 0.028 Mpc, which that the intrinsic spectral behavior of foreground emission corresponds to a kernel of width  $\sim 0.02 \text{ hMpc}^{-1}$ . In this work, our foreground model is to exclude  $k$ -modes smaller than the sum of the maximum realizable delay on a baseline (converted from seconds of light-travel time to  $\text{hMpc}^{-1}$  using equation 8) and this kernel. In effect, this model states that intrinsic spectral structure in foregrounds corrupt  $0.02 \text{ hMpc}^{-1}$  beyond a naïve prediction based only on the physical length of the baseline. We explore the effects of modifying this model in §4.1.

### 3.4. Detecting the HI Power Spectrum

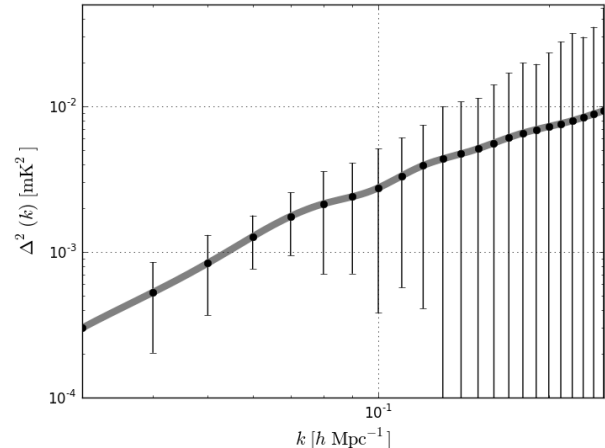


**Figure 9.** Predicted constraints on  $z = 0.89$  21cm power spectrum from a 30 day observation with a 35-tile BAOBAB system. The net result is a  $\sim 5\sigma$  detection of the power spectrum. Results are comparable in the other 2 redshift bins.

The first major science result from BAOBAB will be the detection of the 21cm power spectrum near  $z \sim 1$ . A high significance detection will be achievable with a short  $\sim 1$ -month observation with a 35-tile system operating in the maximum redundancy shown in Figure 6.<sup>22</sup> The predicted measurement for a 30-day observation (240 hours) is shown in Figure 9. These observations assume a 100-MHz bandwidth centered on 750 MHz ( $z = 0.89$ ). The net result is an  $5.4\sigma$  detection of the 21cm power spectrum when our model for foreground emission from §3.3 is used to exclude contaminated modes. Results for bands centered on 650 ( $z = 1.18$ ) and 850 MHz ( $z = 0.67$ ) are similar, yielding  $5.7\sigma$  and  $5.0\sigma$  detections, respectively. The lower significance detection at the lowest redshifts results from the scaling of the angular diameter distance; at redshift  $z = 0.67$ , a  $16\lambda$  baseline corresponds to a  $k_{\perp}$  wavemode of  $\sim 0.06 \text{ hMpc}^{-1}$ , limiting the number of baselines that can probe the largest-scale  $k$ -modes where thermal noise is lowest. Over the  $z = 0.5 - 1.5$  range, both the 21cm signal and, the noise remain roughly constant in magnitude, the latter because it is dominated by a frequency-independent front-end amplifier noise temperature. This trend does not continue indefinitely, however, as sky noise increases with increasing redshift, eventually dominating the system temperature.

Measurements of this significance will allow for an accurate determination of  $f_{\text{HI}} b$ , the combination of the cosmic neutral hydrogen fraction and the bias of neutral hydrogen containing regions, as a function of redshift. Breaking the degeneracy between these parameters will require additional information. Measuring redshift-space distortions can, in principle, separate the effects of the two terms. Constraints from a longer integration or a system with  $\sim 64$  elements will further improve constraints on the neutral hydrogen power spectrum, and it will be possible for these systems to measure redshift-space distortion effects. Measuring these effects accurately re-

<sup>22</sup> Correlator inputs have traditionally been in powers of 2; hence this array is our  $\sim 32$ -tile configuration. The sensitivity calculations do assume that all 35 elements are correlated.

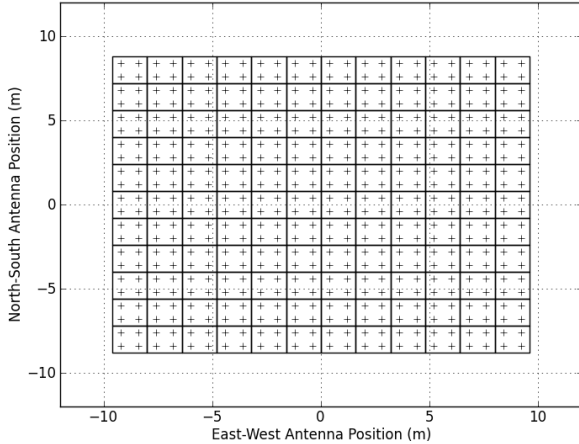


**Figure 10.** The maximum redundancy configuration of a 132-element BAOBAB system. The close-packed tiles are chosen to produce the shortest possible baselines.

quires more careful systematic control, which may warrant different configurations and observing strategies, so we postpone an exploration of this science to a future work (see, e.g., Masui et al. 2010; Masui & McDonald).

### 3.5. Detecting Baryon Acoustic Oscillations

As shown in Figure 8, a 132-tile BAOBAB array with the configuration shown in Figure 10 has effectively reached the sample variance limit in 180 days (1440 hours) of observing time. This observation yields a  $2.9\sigma$  detection of the BAO features at  $z = 1.18$ , with effective  $1.7-$  and  $2.3\sigma$  non-detections at the  $z = 0.67$  and  $z = 0.89$  bands, respectively, where we have isolated the BAO features from the broad-band shape of the power spectrum by removing a model fit using the transfer function from Eisenstein & Hu (1998). The effect of sample variance is most dominant at the lower redshifts, because the angular diameter distance scaling means that fewer samples of the BAO scale can be found in the same area of sky (this observation of 8-independent fields with a  $0.045$  steradian primary beam corresponds to an effective survey area of  $\sim 1200$  square degrees). While longer observations with the same array configuration can improve these constraints by reducing thermal noise on the smaller scale modes, a better approach will be to observe additional independent fields.

For our fiducial BAOBAB observation, we use an array which observes 24 independent fields (i.e., three independent declination observations for 8 hours per day), yielding an effective survey area of  $\sim 3600$  square degrees. We discuss the motivation for this particular approach to increasing survey volume in §4.2. There are several equivalent ways an experiment can probe this additional area. One approach would be to conduct three 1-year surveys, with the dipoles pointed towards a different declination; this could be achieved by physically placing the array on a platform inclined by  $\sim 15^\circ$ , or potentially by adding a steering component to the tile-beamformers. If the beamformers are designed to allow multiple beams, one could in principle achieve similar sensitivities with only one year of observing, although at the expense of additional degrees of complexity in the

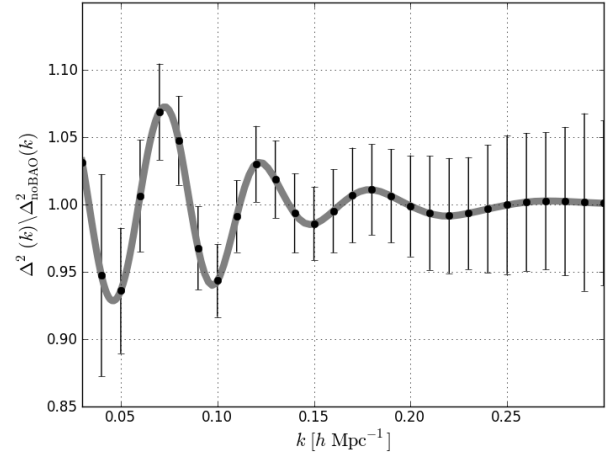


**Figure 11.** Predicted constraints on the  $z = 0.89$  BAO features from a 180 day observation of three-declination fields with a 132-element BAOBAB system. The net result is a  $4\sigma$  detection of the BAO features. The sensitivity is comparable in the other 2 redshift bins.

system. If funding permits, the simplest approach might be to build three 132-tile BAOBAB arrays, each tilted towards a different declination; this would also yield the subsequently predicted sensitivities in only one season of observing. Note that for BAO science these independent configurations are more desirable than an array with a larger number of fully correlated tiles. Since we are using a close-packed configuration, the addition of more tiles can only yield new modes at corresponding larger  $k_\perp$  where the amount of BAO information is significantly diminished. It may be possible that more information could be recovered from these larger  $k$  modes using a reconstruction method (e.g. Eisenstein et al. 2007, Padmanabhan et al. 2009, Noh et al. 2009), but we do not explore this option in this work. In §4.2, we discuss other ways to increase the survey footprint and further reduce the effect of sample variance.

We plot the expected constraints for the three-declination range fiducial BAOBAB observations on the  $z = 0.89$  BAO features in Figure 11, where the broad band shape of the power spectrum has been removed using the transfer function fit of Eisenstein & Hu (1998), which neglects BAO. The measurements from a 180-day integration at each declination range with this array amount to an  $4\sigma$  detection of these features. Results are similar for the other redshift bins, with expected  $3\sigma$  and  $5\sigma$  detections at redshifts of  $0.67$  and  $1.18$ , respectively. While it is clear from Figure 8 that sample variance dominates the errors on the largest scale modes after 180 days of observing one declination range, we find the additional sensitivity towards the higher BAO peaks with this observing duration yields better constraints on the signal than e.g., observing twice as many declination ranges for 90 days.

With a significant BAO detection, BAOBAB can also begin to place constraints on cosmological parameters. To quantify the effect of such measurements, we use the Fisher matrix formalism of the Joint Dark Energy Mission (JDEM) Figure of Merit Science Working Group (FoMSWG; Albrecht et al. 2009), defining our Fisher ma-

trix as:

$$\mathcal{F}_{ij} = \sum_b \frac{1}{\sigma_b^2} \frac{\partial f_b}{\partial p^i} \frac{\partial f_b}{\partial p^j}, \quad (17)$$

where  $f$  is some observable measured at some  $b$  values,  $\sigma^2$  is the variance in a measured value of  $f$ ,  $p^i$  are cosmological parameters, and we sum over all measured  $f_b$  values.

We propagate our power spectrum measurements into constraints on the Hubble parameter  $H(z)$  and angular diameter distance  $D_A$  using this formalism, where  $f = \Delta^2(k)$ , our measured power spectrum,  $b = k$ , the set of  $k$ -modes we measured, and  $p^i = [H(z), D_A]$ . The derivatives with respect to  $D_A$  and  $H(z)$  are straightforward to calculate, as they affect our measurements through the  $X$  and  $Y$  parameters defined in equations 5 and 8. In effect, changing  $H(z)$  or  $D_A$  changes the  $k$ -modes sampled by BAOBAB. For our calculations, we exclude  $k$ -modes deemed contaminated by our foreground model of §3.3. We also model the nonlinear degeneration of higher  $k$ -modes using the elliptical Gaussian formula from Seo & Eisenstein (2007). To isolate the constraints provided by the BAO features from the broad-band shape of the power spectrum, we again remove a model fit using the transfer function from Eisenstein & Hu (1998). We split our data into three redshift bins centered at  $z = 0.67, 0.89$  and  $1.18$ . Although our frequency coverage is continuous between  $z = 0.58$  and  $1.37$ , we find that there is minimal penalty for using only three bins in a Fisher matrix study. The result of this calculation is that our fiducial 3-declination, 180-day integration yields measurements of  $H(z)$  with an error ranging from 10% to 5% across our three redshift bins, from low to high redshift, and measurements of  $D_A$  with errors effectively constant at 18% over the same range (note that errors  $\gtrsim 5\%$  should be understood in the usual formal Fisher matrix sense – these measurements would not correspond to significant detections, taken in isolation). The particularly poor constraints on  $D_A$  come from the loss of modes due to foreground emission; we further explore the effects of our foreground model in §4.1. Taking correlations between  $H(z)$  and  $D_A$  into account, these measurements amount to 2.5% to 4.5% errors on a “dilation factor,” which scales  $D_A$  and  $H^{-1}(z)$  in proportion. Expressed as a single constraint on the  $z \sim 1$  distance scale, these measurements correspond to a dilation factor error of 1.9%. The exact uncertainties are given in Table 2.

It is also straightforward to propagate these errors on  $H(z)$  and  $D_A$  into errors on underlying cosmological parameters through the Fisher matrix formalism of equation 17. In this case,  $f$  is now  $H(z)$  or  $D_A$ , and  $b$  corresponds to the redshift bin it was measured in.  $H(z)$  is given by:

$$H^2(z) = H_0^2 \left[ \Omega_m (1+z)^3 + \Omega_k (1+z)^2 + \Omega_{DE} \exp \left( 3 \int_0^z \frac{dz'}{1+z'} [1 + w(z')] \right) \right]. \quad (18)$$

$D_A$  is given by:

$$D_A(z) = \frac{1}{1+z} \int_0^z \frac{cdz}{H(z)} \quad (19)$$

The parameters of interest,  $p^i$ , are now the underlying cosmological parameters. We use the parameterization of the JDEM FoMSWG, which include  $w_m, w_b, w_k$  and  $w_{DE}$  ( $w_X = \Omega_X h^2$ , where  $m, b, k$ , and  $DE$  correspond to the matter, baryon, curvature and present day dark energy density, respectively) although we use the simpler 2-component form for the dark energy equation of state:

$$w(a) = w_0 + (1 - a)w_a. \quad (20)$$

Following the convention of Dark Energy Task Force report (Albrecht et al. 2006), we marginalize over all other parameters after combining our Fisher matrices with constraints from other experiments, to create  $2 \times 2$  matrix representing constraints on  $w_0$  and  $w_a$ . As a Figure of Merit we use  $\text{FoM} = |\mathcal{F}'|^{1/2}$ , where  $\mathcal{F}'$  is our original Fisher matrix  $\mathcal{F}$ , marginalized to a 2D ( $w_0, w_a$ )-space; this FoM is proportional to the inverse of the error ellipse area in the  $w_0 - w_a$  plane.

As a baseline for current dark energy constraints, we use the JDEM FoMSWG predictions for the Planck satellite, combined with constraints from the BOSS-LRG survey listed in Table 2 and a 5% error on  $H_0$ . This combination of experiments yields an FoM of 8.7. Including the measurements from our fiducial BAOBAB observation increases this FoM value to 16.0. This FoM shows that the high-redshift constraints from BAOBAB can significantly improve our current measurements of the dark energy equation of state. If we include the Ly $\alpha$  forest survey of BOSS, our baseline constraint FoM becomes 17.8 which is improved to 22.5 with the inclusion of BAOBAB data. These constraints are plotted as 1 and  $2\sigma$  error ellipses in Figure 12. Even when the BOSS-Ly $\alpha$  forest constraints between redshifts 2 and 3 are added, BAOBAB still provides valuable information, serving to increase the FoM by  $\sim 25\%$ .

#### 4. DISCUSSION

We break this discussion into two parts. In §4.1, we consider two components of our analysis which may be overly simplistic: our model of the BAOBAB primary beam as a frequency-independent Gaussian, and our foreground emission model. We discuss the effects any shortcomings in these models could have on our conclusions. In §4.2, we consider the fact that sample variance is the dominant source of uncertainty in our measurements, and present future approaches that could improve the dark energy constraints possible with the BAOBAB instrument.

##### 4.1. Potential Shortcomings in the Analysis

A effect that could modify the predictions presented in this work is the use of an overly simplistic model for the BAOBAB beam: a frequency independent Gaussian. Although this model is sufficient to calculate sensitivities, the effects of a more realistic beam model on the delay spectrum foreground removal technique will necessitate further investigations. The principle cause for concern is from the existence of frequency-dependent grating-lobe structure associated with the tile. These sidelobes can introduce apparent frequency structure into otherwise spectrally smooth foreground emission. If this structure represents a significant increase in the size of the delay-space convolving kernel, it will move the foreground contaminated region to higher  $k$  values. If the size of the

**Table 2**

Percent errors on the distance scale from BAO measurements, for a three declination BAOBAB survey. The correlation is the correlation coefficient between the  $H(z)$  and  $D_A$  measurements.  $R$  is the “dilation factor,” a single estimate of the distance scale which scales  $D_A$  and  $H^{-1}(z)$  in proportion. BOSS-LRG constraints come from Schlegel et al. (2009) and BOSS-Ly $\alpha$  Forest constraints come from the method of McDonald & Eisenstein (2007) and Dawson et al. (2012).

Survey	Redshift	$H(z)$ Error	$D_A$ Error	Correlation	$R$ Error
BAOBAB	0.67	9.6%	18.6%	0.72	4.7%
BAOBAB	0.89	6.7%	18.4%	0.74	3.5%
BAOBAB	1.18	4.9%	17.9%	0.74	2.7%
BOSS-LRG	0.35	1.8%	1.0%	0.41	0.7%
BOSS-LRG	0.6	1.7%	1.0%	0.41	0.7%
BOSS-Ly $\alpha$	2.5	3.1%	7.4%	0.58	2.0%

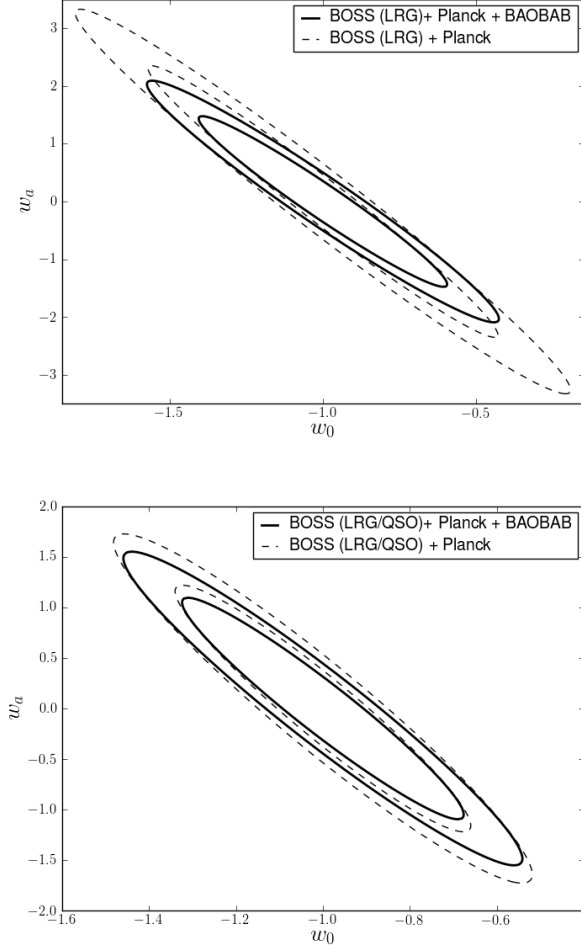


**Figure 12.** 1 and  $2\sigma$  error ellipses in the  $w_0 - w_a$  plane for various surveys. *Top:* The dotted line shows constraints from Planck, BOSS-LRG and a 5% error on  $H_0$ ; the solid line shows the effect of including a 1440-hour integration on three independent declination fields with a 132-tile BAOBAB array. These error ellipses correspond to Figures of Merit of 8.7 and 16.0, respectively. *Bottom:* The same as the left panel, but both constraints now include BOSS-Ly $\alpha$  forest measurements. These error ellipses corresponds to Figures of Merit of 17.8 and 22.5 with and without BAOBAB. Although the high-redshift measurements from the Ly $\alpha$  forest enhance the constraints on  $w_a$ , BAOBAB still provides a significant improvement in the overall FoM.

effect is large enough to push foreground emission on the shortest baselines beyond the first BAO peak, the predicted cosmological constraints could be reduced.

Note, however, that the frequency-independent Gaus-

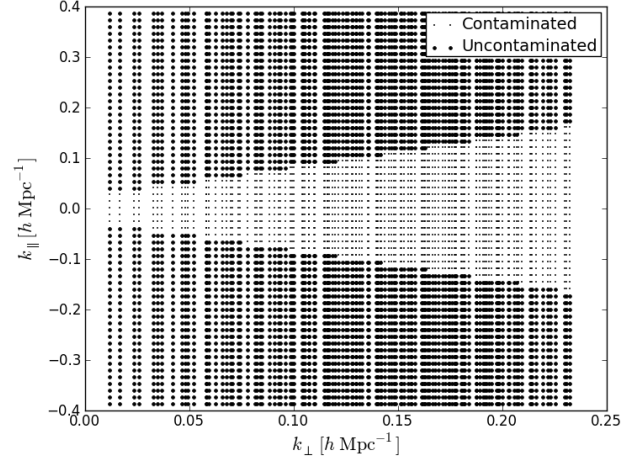


**Figure 13.** The sampling pattern of BAOBAB-132 in the  $(k_\perp - k_\parallel)$ -plane. Modes are marked as either uncontaminated or contaminated by foregrounds using our model of §3.3.

sian beam is not as bad an assumption as it might first appear. If we were trying to image the sky, ignoring the grating lobes associated with the tile would be unjustified. With the delay spectrum approach, though, the issue is not the existence of the sidelobes, but their frequency dependence. If the frequency Fourier transform of the beam pattern is particularly broad — corresponding to rapid evolution of the beam pattern with frequency — then foreground emission will have a similarly broad footprint in delay space, compromising the 21cm signal. However, as argued in P12b, it is difficult for an element only several wavelengths across to possess such frequency structure. As stated in §3.3, we will postpone a detailed investigation of these effects to a future paper, and focus here on array sensitivities, for which the Gaussian model is sufficient.

As noted in §3.5, our constraints on  $D_A$  are significantly limited by foreground emission. We illustrate this effect in Figure 13, which shows the sampling pattern of BAOBAB-132 at 750 MHz in the  $(k_\perp - k_\parallel)$ -plane, highlighting those modes discarded as contaminated by our foreground model of §3.3. Foreground contamination effectively excludes modes where  $k_\perp \lesssim k_\parallel$ , i.e., transverse modes. This has the effect of significantly degrading the achievable constraints on  $D_A$ .

While our foreground model presented in §3.3 is empirically motivated, accurate predictions for foreground emission will need to come from early BAOBAB arrays or other 21cm experiments. We briefly explore the effect of

changing the size of the additive component of our foreground model arising from the spectral smoothness (or lack thereof) the emission. For our fiducial model, this term has a magnitude of  $k_{\parallel} = 0.02 \, h\text{Mpc}^{-1}$ ; as test cases, we analyze the constraints obtainable with BAOBAB if this term is changed by  $\Delta k_{\parallel} = \pm 0.01 \, h\text{Mpc}^{-1}$ . This has the effect of moving the cutoff between contaminated and uncontaminated modes in Figure 13 up or down by  $0.01 \, h\text{Mpc}^{-1}$ .

The effect of increasing this term (i.e., if foreground emission is not as spectrally smooth as predicted) is to degrade the significance of our BAO detections in each of the redshift bins by  $\sim 0.5\sigma$ , our  $H(z)$ ,  $D_A$ , and  $R$  constraints by  $\sim 1$ ,  $\sim 5$ , and  $\sim 0.5 - 1$  percentage points, respectively. Reducing the foreground emission footprint in  $k$ -space (i.e., if foregrounds are spectrally smoother than predicted) has similar effects with the opposite sign: the significance of our BAO detections in each band are increased by  $\sim 0.5\sigma$ , our  $H(z)$ ,  $D_A$ , and  $R$  constraints are improved by  $\sim 0.5$ ,  $\sim 6$ , and  $\sim 0.5$  percentage points, respectively. From this analysis, it is clear that foreground emission can significantly alter the achievable constraints on  $D_A$ , but ultimately, the success of BAOBAB will not be determined by the details of foreground spectral properties.

#### 4.2. Improving Our Constraints

As discussed in §3.5, sample variance dominates the uncertainties in power spectrum measurements from BAOBAB. However, measuring a new set of independent modes is not a trivial undertaking. By using a close-packed array, BAOBAB completely samples the  $uv$ -plane out to some maximum baseline length. Therefore a simple array rotation or reconfiguration will not yield new samples. Furthermore, in our highest redshift bin of  $z = 1.18$ , the longest baseline in the 132-tile array probes a transverse  $k$ -mode of  $k_{\perp} = 0.15 \, h\text{Mpc}^{-1}$  (and at lower redshift, this longest baseline corresponds to an even larger value of  $k_{\perp}$ ). At this scale and smaller, most BAO information is being lost to non-linear damping effects. Therefore, the returns from increasing the array size beyond  $\sim 128$  tiles are limited, since effectively no new modes with significant BAO information will be probed.

As an upper-limit to the constraints obtainable with a single-declination,  $\sim 1200$  square degree, 132-tile BAOBAB observation (as opposed to our fiducial observation targeting three declination fields) we compute the results of a completely sample variance limited survey, i.e., one where thermal noise uncertainties have been set to 0 (although modes are still excluded using our foreground emission model). This sample variance limited 132-tile BAOBAB observation yields a  $z \sim 1$  distance scale uncertainty of  $\sim 1.8\%$  (compared with  $1.9\%$  for our fiducial 1-year observation of 3 independent declination fields). For comparison, a 10-year (14,400 hour), one declination observation with the same array yields a distance scale uncertainty of  $2.2\%$ . Therefore, while better constraints can come from a longer observation, obtaining measurements of new modes to beat down sample variance is clearly the optimal way to proceed. There are two ways forward to achieve this goal: map a different volume of the universe (as with our fiducial experiment) or

recover foreground corrupted modes. We consider each of these approaches in turn.

Since BAOBAB is a zenith-pointing, drift-scanning telescope, to map a new area of the sky, it will either need to be relocated to a different latitude or tilted to point towards a different patch of sky. Either option is potentially feasible, as even a 132-tile BAOBAB experiment spans less than 20 meters. With a primary beam full-width half-max of  $\sim 15^\circ$ , there are  $\sim 10$  independent pointings in declination that BAOBAB can target. Since our fiducial observation already targets three declination fields, mapping every declination could in principle yield  $\sim 70\%$  reductions in the error bars over the results presented.

The other way to potentially measure new modes and beat down sample variance is to recover samples we have considered corrupted by foregrounds. There are two ways foregrounds compromise BAOBAB observations. The first is the limited observing time per-day, set by Galactic emission, which we have treated as irreparably corrupting all samples, even those in principle recoverable with the delay transform. If it is possible to observe all 24 hours of right ascension, as opposed to the 8 considered here, the constraints from a single observing season will increase by a factor of  $\sqrt{3}$ . While it is unlikely that all 24 hours of right ascension will be workable, our fiducial value of 8 hours per day, motivated by observations with present EoR experiments, may well be conservative, since Galactic synchrotron emission has significantly fallen in brightness compared to EoR frequencies.

Even when observing a “cold patch,” foregrounds corrupt large scale  $k$ -modes with a footprint moving to smaller scales as baseline length increases (§3.3). If these modes could be retrieved, they could significantly increase the volume of Fourier space that BAOBAB can probe. As an upper-limit, we calculate the obtainable power spectrum constraints ignoring all foreground contamination. The result is that a 1-year observation of three independent declination fields yields a distance scale uncertainty of  $1.4\%$ , an increase of half a percentage point over the same observation including foreground emission. In particular, we note that a foreground-free observation yields  $\lesssim 5\%$ -level errors on  $D_A$ . While an analysis of foreground removal techniques is beyond the scope of this work, this result suggests that foreground removal may be the way to improve constraints on  $D_A$ .

As an order of magnitude estimate, we can consider whether a foreground removal or subtraction scheme might be more effective in the BAO band than at EoR frequencies. At  $k \sim 0.1 \, h\text{Mpc}^{-1}$ , the 750-MHz BAO 21cm power spectrum reaches  $\sim 3 \times 10^{-3} \, \text{mK}^2$ , compared with a peak brightness at EoR frequencies of 150 MHz reaching  $\sim 10 \, \text{mK}^2$ . The steep spectrum Galactic synchrotron emission has a spectral index of  $-2.5$ , and so will fall by a factor of  $(5^{-2.5})^2 = 3.2 \times 10^{-4}$  in units of temperature squared. (Extragalactic point sources are less steep spectrum, and so will not fall off in brightness as steeply. Therefore, this estimate can be considered a lower limit on the foreground-to-signal ratio). Roughly speaking, then, the foreground-to-signal ratio is unchanged compared with EoR experiments, suggesting that a foreground isolation scheme like the delay-spectrum technique is still likely the most viable ap-



proach for first-generation experiments limited in collecting area.

## 5. CONCLUSIONS

In this work we have presented a concept for a new experiment using the redshifted 21cm line of neutral hydrogen to probe cosmology at  $z \sim 1$ . The BAO Broadband and Broad-beam Array (BAOBAB) will incorporate both the hardware and analysis infrastructure developed for 21cm experiments at higher redshifts.

The hardware design will borrow heavily from the Precision Array for Probing the Epoch of Reionization (PAPER) and the Murchison Widefield Array (MWA), using a scaled version of the PAPER dipoles as a feed element, tiling dipoles as done by the MWA, and modifying the CASPER FPGA/GPU PAPER correlator to perform full dual-polarization cross-correlations of all elements. Significant improvements to the system temperature will be brought about through state-of-the-art uncooled, low-noise amplifiers. Relative to PAPER, the collecting area will be substantially increased through the use of tiles of 4 dipoles combined through a beamformer, as demonstrated by MWA efforts. Although we have largely avoided specific cost-estimates, it is fair to say that this infrastructure is obtainable at a fraction of the cost of the  $\sim 100$ -million dollar ground-based optical redshift surveys.

On the analysis side, BAOBAB will use the maximum redundancy configurations and delay spectrum foreground removal techniques presented in Parsons et al. (2012a) and Parsons et al. (2012b) to enhance sensitivity to Fourier modes along the line-of-sight. Motivated by the science of Baryon Acoustic Oscillations, BAOBAB will utilize extremely close-packed arrays to maximize the number of short baselines. The sensitivity calculations presented here show that BAOBAB will achieve several milestone measurements over our anticipated staged deployment process. A  $\sim 32$ -element BAOBAB system will yield high significance detections of the HI power spectrum, and constrain the evolution of the cosmic neutral hydrogen fraction from  $z = 0.5$  to  $1.5$  as well as the bias of DLAs. Over the same wide redshift range, a  $\sim 128$ -element system will allow for a first detection of the BAO features in the power spectrum, and yield errors on the distance scale  $R$  at the several percent level. When combined with our current constraints on dark energy, including those forthcoming from the BOSS and Planck experiments, BAOBAB's measurements result in substantial increase in the Dark Energy Task Force Figure of Merit, representing constraints on the nature and time evolution of dark energy over a wide range of cosmic history.

## REFERENCES

Adams, J. J., et al. 2011, *ApJS*, 192, 5

- Albrecht, A., et al. 2006, *ArXiv Astrophysics e-prints*  
—, 2009, *ArXiv e-prints*  
Amendola, L., et al. 2012, *ArXiv e-prints*  
Ansari, R., Campagne, J.-E., Colom, P., Magneville, C., Martin, J.-M., Moniez, M., Rich, J., & Yèche, C. 2012a, *Comptes Rendus Physique*, 13, 46  
—, 2012b, *Comptes Rendus Physique*, 13, 46  
Barkana, R., & Loeb, A. 2007, *Reports on Progress in Physics*, 70, 627  
Battye, R. A., Browne, I. W. A., Dickinson, C., Heron, G., Maffei, B., & Pourtsidou, A. 2012, *ArXiv e-prints*  
Chang, T.-C., Pen, U.-L., Bandura, K., & Peterson, J. B. 2010, *Nature*, 466, 463  
Chang, T.-C., Pen, U.-L., Peterson, J. B., & McDonald, P. 2008, *Physical Review Letters*, 100, 091303  
Clark, M. A., La Plante, P. C., & Greenhill, L. J. 2011, *ArXiv e-prints*  
Dawson, K. S., et al. 2012, *ArXiv e-prints*  
Drinkwater, M. J., et al. 2010, *MNRAS*, 401, 1429  
Eisenstein, D. J., & Hu, W. 1998, *ApJ*, 496, 605  
Eisenstein, D. J., Hu, W., & Tegmark, M. 1998, *ApJ*, 504, L57  
—, 1999, *ApJ*, 518, 2  
Eisenstein, D. J., Seo, H.-J., Sirko, E., & Spergel, D. N. 2007, *ApJ*, 664, 675  
Eisenstein, D. J., et al. 2005, *ApJ*, 633, 560  
Ellis, R., et al. 2012, *ArXiv e-prints*  
Jacobs, D. C., et al. 2011, *ApJ*, 734, L34  
Kaiser, N. 1987, *MNRAS*, 227, 1  
Larson, D., et al. 2011, *ApJS*, 192, 16  
Lewis, A., Challinor, A., & Lasenby, A. 2000, *ApJ*, 538, 473  
Lonsdale, C. J., et al. 2009, *IEEE Proceedings*, 97, 1497  
Madau, P., Meiksin, A., & Rees, M. J. 1997, *ApJ*, 475, 429  
Masui, K. W., McDonald, P., & Pen, U.-L. 2010, *Phys. Rev. D*, 81, 103527  
McDonald, P., & Eisenstein, D. J. 2007, *Phys. Rev. D*, 76, 063009  
Morales, M., & Wyithe, J. 2010, *Annual Review of Astronomy and Astrophysics*, 48, 127  
Morales, M. F. 2005, *ApJ*, 619, 678  
Noh, Y., White, M., & Padmanabhan, N. 2009, *Phys. Rev. D*, 80, 123501  
Padmanabhan, N., White, M., & Cohn, J. D. 2009, *Phys. Rev. D*, 79, 063523  
Parsons, A., Pober, J., McQuinn, M., Jacobs, D., & Aguirre, J. 2012a, *ApJ*, 753, 81  
Parsons, A., et al. 2008, *PASP*, 120, 1207  
Parsons, A. R., & Backer, D. C. 2009, *AJ*, 138, 219  
Parsons, A. R., Pober, J. C., Aguirre, J. E., Carilli, C. L., Jacobs, D. C., & Moore, D. F. 2012b, *ApJ*, 756, 165  
Parsons, A. R., et al. 2010, *AJ*, 139, 1468  
Peterson, J. B., Bandura, K., & Pen, U. L. 2006, *ArXiv Astrophysics e-prints*  
Pober, J. C., et al. 2012, *AJ*, 143, 53  
Pritchard, J. R., & Loeb, A. 2011, *ArXiv e-prints*  
Schlegel, D., White, M., & Eisenstein, D. 2009, in *Astronomy, Vol. 2010, astro2010: The Astronomy and Astrophysics Decadal Survey*, 314+  
Schlegel, D., et al. 2011, *ArXiv e-prints*  
Seo, H.-J., Dodelson, S., Marriner, J., McGinnis, D., Stebbins, A., Stoughton, C., & Vallinotto, A. 2010, *ApJ*, 721, 164  
Seo, H.-J., & Eisenstein, D. J. 2007, *ApJ*, 665, 14  
Wright, E. L. 2006, *PASP*, 118, 1711  
Wyithe, J. S. B., Loeb, A., & Geil, P. M. 2008, *MNRAS*, 383, 1195  
Zwaan, M. A., Meyer, M. J., Staveley-Smith, L., & Webster, R. L. 2005, *MNRAS*, 359, L30